Characteristics of airborne gold aggregates generated by spark discharge and high temperature evaporation furnace: Mass–mobility relationship and surface area

C.R. Svensson [a,*], L. Ludvigsson [b], B.O. Meuller [b], M.L. Eggersdorfer [c], K. Deppert [b], M. Bohgard [a], J.H. Pagels [a], M.E. Messing [b], J. Rissler [a]

[a] Ergonomics and Aerosol Technology, Lund University, Box 118, SE-22100 Lund, Sweden
[b] Solid State Physics, Lund University, Box 118, SE-22100 Lund, Sweden
[c] Experimental Soft Condensed Matter, Harvard University, Cambridge, MA 02138, USA

ARTICLE INFO

ABSTRACT

The properties of gas-borne aggregates are important in nano-technology and for potential health effects.

Gold aggregates from three generators (one commercial and one custom built spark discharge generator and one high-temperature furnace) have been characterized. The aggregate surface areas were determined using five approaches – based on aggregation theory and/or measured aggregate properties. The characterization included mass-mobility relationships, effective densities (assessed by an Aerosol Particles Mass analyzer), primary particle analysis (based on Transmission Electron Microscopy), as well as total mass and number concentration outputs.

The relationships between mass and mobility are well described by power-law functions with exponents of 2.18–2.35. For all generators, the primary particles of the aggregates were fused together by a bridge with a diameter typically ~60–70% of the primary particle diameter (5–10 nm). The total mass outputs were 6.1–48.1 mg/m3 and the predicted surface area outputs in the range 0.9×10^{-3}–17×10^{-3} cm^2/cm^3.

The aggregate effective densities differed considerably between generators. The difference could partly be explained by the differences in primary particle diameter, but not fully. This in turn may be explained either by a varying primary particle size with aggregate size, or by that there are slight differences in the morphology of the aggregates from the generators.

1. Introduction

The properties of airborne agglomerates and aggregates are important for many reasons. It is known that exposure to airborne particulates, which often includes agglomerates/aggregates, can have adverse health effects (Barath et al., 2010; Dockery et al., 1993). To understand the toxicological effect of inhaling aggregates it is important to (I) have robust but variable methods available for controlled generation of airborne aggregates (for controlled toxicological tests) and (II) methods assessing the critical properties of the aggregated particles. Studies have shown that for various particle types the surface areas of the particles produce coherent dose-response relations, suggesting that the promoter of toxicity is the surface area rather than the mass or particle number inhaled (Aitken, Chaudhry, Boxall, & Hull, 2006; Donaldson et al., 2008; Waters et al., 2009). Hence it is of great importance to have readily available tools and models for calculating the surface area dose for aggregated particles, be it in a lab during toxicological studies, occupational exposure setting, or for other applications.

Apart from surface area of the aggregates/agglomerates, produced by for example flame spray pyrolysis, high temperature evaporation condensation or spark discharge, there are several other aggregate properties that needs to be thoroughly characterized such as the mass–mobility relationships, number/mass output, primary particle size (Dillon, Copley, Koos, Bishop, & Grobert, 2013; Heurlin et al., 2012; Messing, Dick, Wallenberg, & Deppert, 2009; Shin et al., 2009).

In this study, the term "agglomerates" is used when primary particles are held together by weak van der Waals forces, and "aggregates" is use for primary particles more strongly bound together by partial melting (DFG, 2013; Lövestam et al., 2010). We here let aggregate include agglomerates if we do not know which nomenclature if most descriptive. Note that the nomenclature of the structures is not used unambiguously in the literature and the two terms can be used interchangeably depending on the research field.

Assessing the surface area of non-spherical nanoparticles is not straightforward, and as of today there few ways of performing direct measurements. For most methods used the measured surface area will be intimately related to the method by which it was determined. Although methods that measure surface area on-line are available (Asbach, Fissan, Stahlmecke, Kuhlbusch, & Pui, 2009; Fierz, Houle, Steigmeier, & Burtscher, 2011; Ntziachristos, Giechaskiel, Ristimäki, & Keskinen, 2004; Wang et al., 2010), these were typically not developed for non-spherical and porous particles, and thus do not work in an optimal way for all types of aggregates (LeBouf et al., 2011). Also there is data suggesting that the techniques based on unipolar diffusion charging does not relate directly to the surface area of the aerosol particles as suggested (Gopalakrishnan, Thajudeen, Ouyang, & Hogan, 2013; Ku & Kulkarni, 2012; Ku & Maynard, 2005). Transmission electron microscopy (TEM) imagery is often used to characterize primary particle size (d_{pp}) of aggregates. On-line techniques such as the aerosol particle mass analyzer (APM) that coupled in a series after a differential mobility analyzer (DMA) determines the mass–mobility relationship, as well as particle effective density (ρ_{effd}), with a relatively high resolution in both time and size (Ehara, Hagwood, & Coakley, 1996; Olfert, Symonds, & Collings, 2007). This technique also allows one to distinguish between externally mixed particles of different effective densities (McMurry, Wang, Park, & Ehara, 2002; Rissler et al., 2014). Various techniques have been used for specific surface area characterization, whereof nitrogen adsorption, or Brunauer Emmett Teller (BET) is the most common (Brunauer, Emmett, & Teller, 1938). BET has been successfully used for nanoparticle surface area characterization (Eggersdorfer, Groehn, Sorensen, McMurry, & Pratsinis, 2012; Ku & Kulkarni, 2012). However, the technique can prove challenging for many applications and nanoparticle sources since it is offline and a relatively large amount of material is needed (min. ~10 mg). Furthermore, the whole particle population collected over a long period of time is characterized, as a whole.

TEM imagery has also been compared to BET measurements and suggested as a stand-alone off-line method for determining specific surface area (Bau, Witschger, Gensdarmes, Rastoix, & Thomas, 2010). A combination of on-line and off-line techniques have also been suggested for the determination of surface area of aggregates, such as that of combining aerosol particle mass measurements (DMA–APM) and basic TEM imagery (Rissler et al., 2012, 2013; Thajudeen, Jeon, & Hogan, 2015).

Another approach to assess surface area is from a theoretical point of view, combined with on-line or off-line techniques. An extensive effort have been made in the area of modeling properties of fractal structures formed by diffusion limited cluster aggregation (DLCA), mainly focusing on number of primary particles in aggregates in relation to the aggregate radius of gyration or mobility size (Chan & Dahneke, 1981; Eggersdorfer, Groehn, Sorensen, McMurry, & Pratsinis, 2012; Meakin, Donn, & Mulholland, 1989; Sorensen, 2011). Furthermore, effort has been devoted to linking the mobility of aggregates to results from image analysis using TEM (Thajudeen et al., 2015). Eggersdorfer, Groehn, Sorensen, McMurry, and Pratsinis (2012) suggest predicting surface area from DMA–APM measurements solely – for aggregates formed by DLCA. There is also considerable work put into describing the properties of aggregates by using a purely theoretical approach (Chan & Dahneke, 1981; Dahneke, 1982).

The aim of this study is to compare number, mass and surface area output concentrations of gold aggregates generated by three methods. These methods were a high temperature furnace (HT), a commercial spark discharge generator (SDG_P), and a novel in-house constructed spark discharge generator (SDG_C). This was accomplished by a detailed characterization regime in combination with theory and semi-empirical models. The instruments used for characterization were: a transmission electron microscopy (TEM), a Differential mobility analyzer – aerosol particle mass analyzer (DMA–APM), and a differential mobility particle sizer (DMPS).
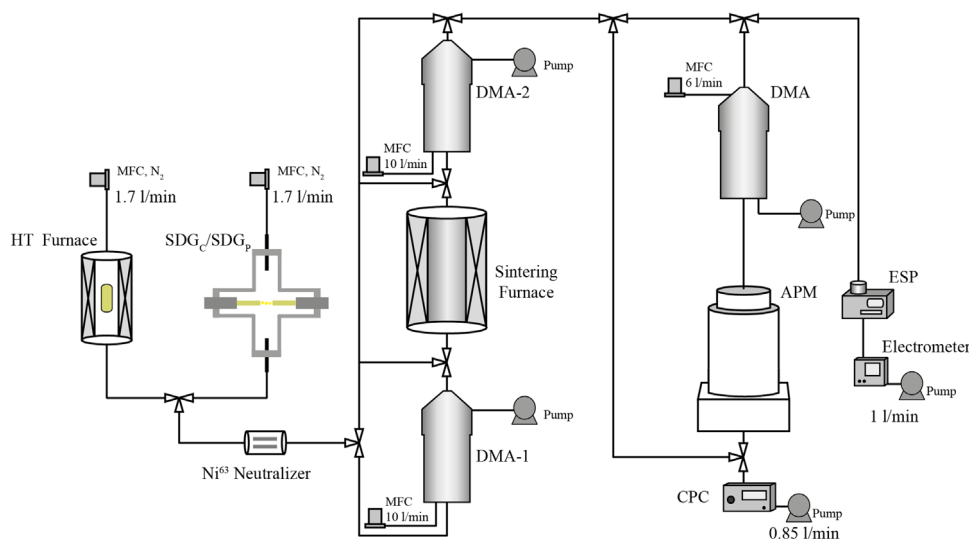
Fig. 1. Overview of the generation and characterization system for the Au aerosols by spark discharge and high temperature evaporation.

The measured particle characteristics were used in combination with 5 approaches to estimate the total surface area output of the generators. The approaches are based on the combination of on-line and off-line techniques and aggregation models:

(I) Mass–mobility data in combination with TEM imagery.
(II) Theory describing the mass of aggregates in combination with TEM imagery.
(III) Mass–mobility data in combination with semi-empirical theory.
(IV) Lall and Friedlander (2006) theory in combination with TEM imagery.
(V) Assumption of spherical particles.

In addition to the primary aim, size dependent properties of the aerosols were determined and compared. These properties include primary particle diameter, bridging between the primary particles, the size dependent effective density, the mass–mobility relationship, and aggregate number size distributions.

The systems have been applied in several biological applications such as deposition in biological fluids studying aggregation and protein corona (Svensson et al., 2013). The HT and SDG$_P$ has also been evaluated with regards to surface area and mass output for air liquid interface studies (Messing et al., 2012). The SDG$_C$ has recently been used in in vivo inhalation studies (manuscript).

The data that this study is based upon is publicly available through Swedish National Data Service (SND, www.SND.gu.se/en) by doi:10.5878/002624.

2. Material and methods

2.1. System setup

The particles were generated using three different systems: a commercially available spark discharge unit, SDG$_P$ (Palas CFG 1000), a custom built spark discharge unit, SDG$_C$, and a high temperature evaporation/condensation furnace (HT) (Scheibel & Porstendorfer, 1983). The setup included a β-emitting ^{63}Ni source (Neutralizer) (Wiedensohler, 1988); two differential mobility analyzers (one long TSI Inc. model 3081) and a custom built Vienna type DMA (Knutson & Whitby, 1975) allowing the selection of a quasi-monodisperse aerosol; a sintering tube furnace (Karlsson et al., 2005) for sintering of aggregates into spherical particles (SINT); an aerosol particle mass analyzer (APM, Kanomax model APM-3600) (Ehara et al., 1996) in series after a DMA; an electrometer (TSI Inc. model 3068B) and a condensation particle counter (CPC) (model 3760, TSI Inc.) for particle detection; and an electrostatic precipitator (ESP)(Deppert, Schmidt, Krinke, Dixkens, & Fissan, 1996) for collection of the particles unto TEM grids. An overview of the generation system is presented in Fig. 1.

The aerosol flow rate was held constant throughout the main part of the system at 1.7 l/min. The flow rate through the SDG$_C$ is variable but here kept at 1.7 l/min and for SDG$_P$ set at either 2.9 or 3.7 l/min. The excess flow rate over 1.7 l/min was released into the atmosphere through a filter. The flow rate for the HT was constant at 1.7 l/min. The aerosol flow through the APM and the CPC was 0.85 l/min and the remaining flow was led through the electrometer and/or ESP. At any given time during experiments aggregates where only characterized or sampled from one of the generation methods i.e. HT, SDG$_C$ or SDG$_P$.

2.2. Particle generation

The SDG$_P$ system was originally designed for the controlled generation of soot particles using graphite electrodes. The systems has a variable carrier gas flow rate and the spark generation frequency can be varied between 0 and 300 Hz (Schwyn, Garwin, & Schmidtott, 1988). For the course of our experiment the system was refitted with gold electrodes and the carrier gas flow was nitrogen gas, >99.9% in purity (Messing et al., 2009), the carrier gas was the same for the SDG$_C$ and HT experiments. During operation, the inter electrode distance in SDG$_P$ are controlled automatically via the discharge voltage, which may change with a changed carrier gas flow. For the SDG$_P$ two different carrier gas flows were used (2.9 and 3.7 l/min).

The SDG$_C$ was designed based on the principle of the SDG$_P$ but with implementations from previous work (Meuller et al., 2012; Tabrizi, Xu, van der Pers, Lafont, & Schmidt-Ott, 2009; Tabrizi, Xu, van der Pers, & Schmidt-Ott, 2010; Tabrizi, Ullmann, Vons, Lafont, & Schmidt-Ott, 2009). The SDG$_C$ was designed to be able to deliver oxide free metal nanoparticles and has therefore a need to be more leak tight compared to the SDG$_P$, and hence, was designed with all vacuum compatible parts made of stainless steel. The chamber and power feed were redesigned to increase control over generation parameters, such as electrode distance, charging current, electrical capacitance, and gas flows. The inter-electrode distance control was improved in SDG$_C$ by the adding a manual linear actuator to the ground electrode. This enables electrode distance adjustments before and during operation. Furthermore, the energy per discharge was increased as well as discharge frequency, creating a larger particle output. In this study, the SDG$_C$ was not running on settings generating the maximal output. SDG$_C$ is a mobile, single unit instrument with all post particle production processing built in. The SDG$_C$ was fitted with gold electrodes for the course of this study.

The HT system utilizes high temperature evaporation of bulk material inside a graphite cylinder, followed by nucleation and aggregation as the temperature decreases. The HT system uses a constant carrier gas flow of 1.7 l/min while two different generation settings were achieved by using two different furnace temperatures of 1575 °C and 1625 °C, these two settings are in this study referred to as HT 1575 and HT 1625. For the course of the experiments in this study the bulk material in the HT was gold.

2.3. DMPS measurements

Differential mobility particle sizer (DMPS) measurements were performed on all aerosols generated. Scans were performed using DMA1 in the set-up in combination with an electrometer, Fig. 1. The aerosol particles were lognormal distributed and the count median diameter (CMD), geometrical standard deviation (GSTD) and total particle number were calculated.

2.4. DMA–APM measurements

The DMA–APM was used for on-line mass determination of mobility-classified particles. A DMA selects particles of one mobility diameter at a time and the mass distribution of the selected particles is determined by the APM. The APM consists of two concentric cylinders rotating at the same angular speed, where the particles are kept in orbit by an electric field (Ehara et al., 1996). Only particles of a specific mass to charge ratio passes the APM and is quantified by the CPC.

$$\frac{m}{q} = \frac{V}{r_c^2 \cdot \omega^2 \cdot \ln\left(\frac{r_2}{r_1}\right)} \tag{1}$$

where r_c is defined as

$$r_c = \frac{(r_1 + r_2)}{2} \tag{2}$$

here m is the particle mass, V is the voltage between the rotating cylinders, ω is the angular velocity, q is the elemental charge, and r_1 and r_2 are the inner and outer cylinder diameter, respectively.

During each APM scan, the mass distribution of the quasi mono disperse particles selected by the DMA was determined by stepping the APM voltage while keeping the rotational speed constant. The voltage at which the distribution peaks was determined by fitting a normal distribution function to the spectra. This is equivalent to how the analysis was done in previous studies of unimodal mass distributions (Rissler et al., 2012, 2013). The particle mass was determined by inserting the fitted voltage into Eq. (1), assuming singly charged particles. For aggregated particles doubly charged aggregates might lead to artifacts (Rissler et al., 2013). The effect of doubly charged particles was investigated prior to the analysis but proved not to be an issue, mainly due to the relatively small aggregate size distribution. The effects of doubly charged particles are mainly governed by the aggregate particle number size distribution and the size selected by the DMA.

For the SDG$_P$ and HT, the APM measurements were performed on monodisperse aerosol fractions in the size range 15–80 nm selected with DMA1. For the SDG$_C$ particles selected covered the size range 40–300 nm. For those measurements a DMA (Model 3071, TSI Inc.) was used for the selection of monodisperse size fractions.

Suspensions of spherical polystyrene latex particles (PSL, Duke Scientific Inc., USA) of sizes 50, 80, 150, 250 and 350 nm were nebulized with an atomizer (Model 3076, TSI Inc.) and used for calibrating the DMA–APM according to the procedure
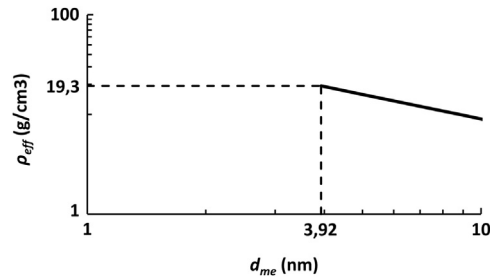
Fig. 2. Principle of the method for primary particle size determination from DMA–APM, as proposed in Charvet et al. (2014).

described by McMurry et al. (2002). During the calibration, the known inherent density of 1.05 g/cm³ was used to determine the DMA–APM correction factor.

2.5. Primary particle analysis

The aggregate primary particles were analyzed concerning size and bridging/necking. Furthermore, the primary particle diameter was estimated from DMA–APM data according to methods described in Charvet, Bau, Paez Coy, Bémer, and Thomas (2014) and Eggersdorfer, Groehn, Sorensen, McMurry, and Pratsinis (2012).

2.5.1. Primary particle size from TEM analysis

Monodisperse aggregates of mobility diameter (d_{me}) 60 nm were selected using a DMA for each of the generation method settings. The aggregates were deposited onto carbon coated Cu TEM grids glued onto semiconductor silicon substrates and analyzed by TEM using an electrostatic precipitator (ESP). The rationale behind depositing only 60 nm nanoparticles was a trade-off suiting all generators with varying distributions and output of the aggregates generated.

A total of 310–604 primary particles for each of the generation method settings were analyzed using ImageJ software (Rasband, 1997–2012). The average (μ) of the cumulative distributions was determined numerically for the number weighted, surface area weighted, and mass weighted primary particle size distributions. Also based on the primary particle distribution the Sauter primary particle size was calculated ($d_{va\text{-}TEM}$):

$$d_{va-TEM} = \frac{\sum \left(N_{pp(d_{pp})} \cdot d_{pp}^3 \right)}{\sum \left(N_{pp(d_{pp})} \cdot d_{pp}^2 \right)} \tag{3}$$

where N_{pp} is the number of primaries quantified.

2.5.2. Primary particle size from DMA–APM

As suggested in Charvet et al. (2014) the primary particle diameter can be estimated by extrapolating the mass–mobility relationship according to a fitted power-law from the bulk density of gold (d_{APM}), Fig. 2. The uncertainty in d_{APM} was also quantified based on the extrapolation.

Eggersdorfer, Groehn, Sorensen, McMurry, and Pratsinis (2012) also suggest a method to determine d_{pp} from DMA–APM data ($d_{va\text{-}APM}$) described in Section 3.2.4. Note that the method suggested in Approach I for estimation of surface area from DMA–APM does only use DMA–APM for mass estimation while TEM-imaging for primary particle size.

2.5.3. Bridging/necking

The degree of bridging between the primary particles was determined for all five conditions investigated. This was performed by measuring the width of the bridge and the two adjacent primary particles (Fig. 3A).

The diameter of the bridge (d_b) was only measured when two clearly identifiable primary particles could be seen on either side, referred to Eq. (4) as d_{pp1} and d_{pp2}. The degree of bridging, the bridging ratio, b_r, was determined as:

$$b_r = \frac{d_b}{\left(\frac{d_{pp1} + d_{pp2}}{2} \right)}. \tag{4}$$

3. Theory and models

This section describe the methodology in quantifying and calculating the mass–mobility relationship, the effective density and the dynamic shape factor. Furthermore, the four approaches used for calculating the surface area for aggregates and for the aggregate distributions are presented. The methods used here are partly based on diffusion limited cluster aggregates (DLCA) according to Eggersdorfer, Groehn, Sorensen, McMurry, and Pratsinis (2012), Lall, Rong, Mädler, and
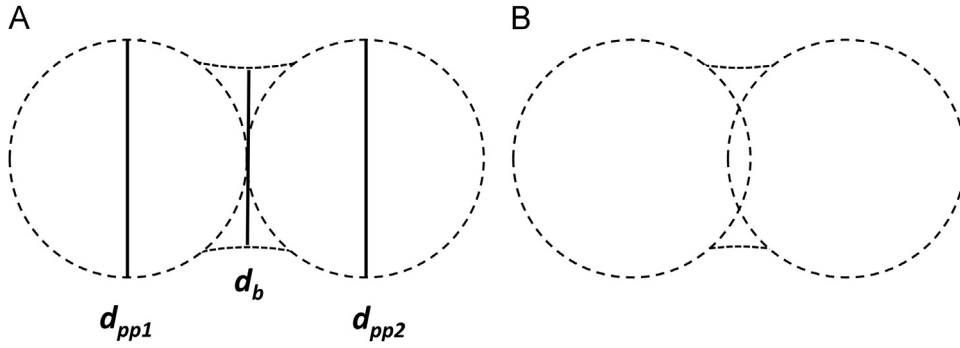
Fig. 3. Principle for bridging determination of the aggregates. (A) and (B) illustrate two ways of approaching the how the bridging between the primaries is formed – either by material condensing after agglomeration (A) or by fusing after agglomeration (B). The two geometries are used in the bridging sensitivity study.

Friedlander (2008) and Sorensen (2011). Furthermore, a method proposed by Rissler et al. (2013) is also used that is not restricted to aggregates formed by DLCA, but would apply to all types of aggregates. In short, this latter approach suggests to estimate the primary particle size is obtained by TEM and combined this with the aggregate mass measured by DMA–APM to calculate its corresponding surface area. This is similar to the method suggested by Bau et al. (2010) with the difference that the aggregate number of primaries (or related to mass when knowing the density of the primary particles) was estimated from aggregation theory.

3.1. The mass–mobility relationship, effective density and shape factor

Numerous studies have shown that the relation between the mobility diameter (d_{me}) and the mass of airborne aggregates formed by diffusion can be described by a power law (such as Park, Kittelson, and McMurry (2004), Rissler et al. (2013)) according to

$$m_{agg}(d_{me}) = k \cdot d_{me}^{D_{mm}} \tag{5}$$

D_{mm} is here referred to as the mass–mobility exponent (in previous studies often referred to as the fractal/mass-fractal dimension), the k in the mass mobility relation is in this study referred to as k-factor.

The effective density (ρ_{eff}) and shape factor (χ) were calculated from the mass–mobility relationship measured by the DMA–APM. The ρ_{eff} is calculated as the ratio of the aggregate mass over the mobility equivalent volume:

$$\rho_{eff} = \frac{6 \cdot m_{agg}(d_{me})}{\pi \cdot d_{me}^3} \tag{6}$$

The χ is calculated as the ratio of the Stokes force (F), or friction factor (f) multiplied by velocity (V), for aggregates (F_{agg}) over volume equivalent spheres (F_{ve}) according to

$$\chi = \frac{F_{agg}}{F_{ve}} = \frac{f_{agg} \cdot V}{f_{ve} \cdot V} = \frac{d_{me} \cdot C_{ve}}{d_{ve} \cdot C_{agg}} \tag{7}$$

The Cunningham slip correction, C, is calculated for the aggregates mobility size, d_{me}, and volume equivalent, d_{ve}, respectively.

3.2. Surface area content

By combining the size dependent surface area of a single aggregate, $SA_{agg}(d_{me})$, (achieved through the three approaches described below) with the mobility number distribution of the corresponding aerosol, the surface area distribution can be calculated:

$$dSA_{agg}/d\log d_{me} = SA_{agg}(d_{me}) \cdot dN/d\log d_{me} \tag{8}$$

The total surface area of the aerosol, SA, is calculated by summing the surface area of each size interval according to

$$SA = \sum \frac{dSA_{agg}(d_{me})}{d\log d_{me}} \cdot d\log d_{me} \tag{9}$$

The total mass of the aerosols can be calculated in the same fashion by replacing SA_{agg} with m_{agg} in Eq. (8) and performing the calculation in Eq. (9).

In addition to the three approaches presented in Sections 3.2.2–3.2.5 the surface area was calculated by assuming the mobility diameter was equal to the geometric diameter i.e. assuming that the particles were spherical. For each method and setting the Au aerosol size distribution was used to calculate the total surface area using the described models/approaches.

3.2.1. Specific surface area – SSA

The specific surface area is in Approaches I and II estimated from analysis of TEM imagery (SSA_{TEM}) using the method proposed in Bau et al. (2010). The method does to the first approximation not consider overlap of the primaries. $d_{va\text{-}TEM}$ is calculated from the primary particle distribution as described in Eq. (3), and SSA_{TEM} according to

$$SSA_{TEM} = \frac{6}{\rho_{Au} \cdot d_{va-TEM}}. \tag{10}$$

3.2.2. Approach I – Bau and Rissler

By multiplying the TEM-derived specific surface area, SSA_{TEM}, by the size dependent aggregate mass, achieved through the DMA–APM measurements, $SA_{agg}(d_{me})$ is calculated for the aggregates as a function of mobility diameter according to

$$SA_{agg}(d_{me}) = SSA_{TEM} \cdot m_{agg}(d_{me}) \tag{11}$$

The method was first suggest by Rissler et al. (2012) and is not restricted to work for aggregates formed by DLCA, but would apply to all types of aggregates – also those formed by dustiness.

3.2.3. Approach II – Bau and Sorensen

A general theoretical approach is suggested in Sorensen (2011) for the calculation of the primary particle number in aggregates. The primary particle number, as function of mobility size, can then be translated into both mass and surface area.

For fractal aggregates formed by DLCA, as in the experiments of this study, the relationship between the aggregate primary particle numbers N, d_{me} and d_{pp} in the free molecular regime is proposed to be

$$d_{me} = d_{pp} \cdot N^{0.46} \tag{12}$$

In the slip transition regime for Knudsen number ($0.1 < Kn < 10$) the following relation between d_m, d_{pp} and N is suggested:

$$d_{me} = d_{pp} \cdot \left(10^{-2 \cdot x + 0.92}\right) \cdot N^x \tag{13}$$

where x is calculated, from the Kn of the mobility diameter and mean free path as

$$x = 0.51 \cdot Kn^{-0.043} \tag{14}$$

By multiplying the aggregate mass (achieved from the number of primaries multiplied by their individual mass) with SSA_{TEM}, the surface area of the aggregate is calculated as

$$SA_{agg}(d_{me}) = SSA_{TEM} \cdot m_{agg}(d_{me}) = SSA_{TEM} \cdot N(d_{me}) \cdot m_{pp}$$
$$= SSA_{TEM} \cdot N(d_{me}) \cdot \left(\frac{\rho_{AU} \cdot \pi \cdot d_{pp}^3}{6}\right) \tag{15}$$

For the calculation of primary particle mass, m_{pp}, the surface area weighted, d_{pp}, from the TEM analysis was used, as was the bulk gold density 19.3 g/cm³ (ρ_{AU}).

3.2.4. Approach III – Eggersdorfer

This approach utilize DLCA theory and DMA–APM data to calculate the surface area of the aggregates (Eggersdorfer, Groehn, Sorensen, McMurry, & Pratsinis, 2012). The approach uses the Sauter diameter of the primary particles, $d_{va\text{-}APM}$, calculated as

$$d_{va} = \cdot \left(\frac{k_a \cdot \pi}{6 \cdot v} \cdot d_{me}^{(2 \cdot D_a)}\right)^{1/(2D_a - 3)} \tag{16}$$

The factors k_a and D_a are based on simulations of DLCA aggregates and are for this study set to 1 and 1.08, respectively. v is the aggregate volume determined from DMA–APM. The SSA_{APM} is then calculated as

$$SSA_{APM} = \frac{6}{\rho_{Au} \cdot d_{va}} \tag{17}$$

The aggregate surface area is calculated as the product of the SSA_{APM} and the aggregate mass from DMA–APM

$$SA_{agg}(d_{me}) = SSA_{APM} \cdot m_{agg}(d_{me}) \tag{18}$$

The principle of the method is tested and valid for both diffusion limited and ballistic aggregation in the transition regime, it is also valid for degrees of sintering up to compact spheres. However, the constants used in Eq. (16) would then be different. The main assumption of the model is that the projected surface area of the aggregates, in the transition regime, is proportional to the drag force.

3.2.5. Approach IV – Lall and Friedlander mass and surface area

Another theoretical approach suggested for estimating aggregate mass and surface area, based on relating the migration velocity of spheres to that of aggregates with similar mobility, was suggested by Lall and Friedlander (2006) and Lall et al. (2008).

In this approach the total number of primary particles in an aggregate is calculated as

$$N(d_{me}) = \frac{12 \cdot \pi \cdot \lambda \cdot d_{me}}{c* \cdot d_{pp}^2} \tag{19}$$

The aggregate mass is then calculated as the number of primaries multiplied by their individual mass:

$$m_{agg}(d_{me}) = N(d_{me}) \cdot \rho \cdot \frac{\pi \cdot d_{pp}^3}{6} = \frac{2 \cdot \rho \cdot \pi^2 \cdot \lambda \cdot d_{pp} \cdot d_{me}}{c*} \tag{20}$$

Similarly, the aggregate surface is calculated as the number of primaries multiplied by their individual surface area

$$SA_{agg}(d_{me}) = SSA_{TEM} \cdot m_{agg}(d_{me}) = SSA_{TEM} \cdot \frac{2 \cdot \rho \cdot \pi^2 \cdot \lambda \cdot d_{pp} \cdot d_{me}}{c*} \tag{21}$$

The dimensionless drag force is denoted as $c*$. The mass and surface area distributions for the aerosols are then calculated using Eqs. (8) and (9).

The method is described as valid if the primary particle radius is much smaller than the mean free path; also bridging is neglected as well as shielding. Shielding is a phenomenon where part of the primary particles do not contribute to the Stokes drag of an aggregate.

For the calculation of primary particle mass, m_{pp}, the surface area weighted, d_{pp}, from the TEM analysis was used, as was the bulk gold density 19.3 g/cm^3 (ρ_{AU}).

4. Sensitivity analysis of bridging on specific surface area

In Approaches I and II, the calculation of surface area is based on the assumption that the primary particles in the aggregates are at point contact. Thus, the specific surface area is determined solely by the surface area of the primary particles – assuming aggregates following previous definitions (Lövestam et al., 2010). Since TEM images show that there are bridging between the primary particles, this is obviously an erroneous assumption. The ratio between the diameter of the bridge and the diameter of the adjacent primary particles is quantified by TEM image analysis.

To test the effect of bridging when determining the surface area according to Approach I (would result in similar effect in Approach II), described in Section 3.2.2., two geometrical views were compared. In method A we assume that the primary particles collide and that the bridge builds up as material condenses unto the aggregate (Fig. 3A), and in method B we assume that two primary particles collide and "melt" together (Fig. 3B). That means that the mass of the bridge is constituted of mass from the primary particles. It might be that the two methods describe aggregates formed in different processes. Likely gold particles, as used in this study, are described by method B.

5. Results and discussion

5.1. Aggregate characteristics

Results include total surface area and mass output, number size distribution and properties related to the mass–mobility relationships. The mass–mobility relationship is described by fitting D_{mm} and k in the associated power law, Eq. (5). The primary particle analysis is presented regarding size and bridging/necking. A sensitivity analysis of the specific surface area of aggregates is performed with regards to bridging between the primaries.

Examples of typical TEM images are shown in Fig. 4. A first order comparison of the aggregates analyzed show that all the methods and settings produce similar structures.

5.1.1. On-line characterization and surface area

For the SDG$_P$, the aerosol distribution statistics are not greatly affected by a change in the carrier gas flow rate from 2.9 to 3.7 l/min, while retaining the same spark generation frequency. To achieve a noticeable effect on particle size distribution, the carrier gas flow rate has to be increased or decreased to the extent that the coagulation rate is affected (Messing et al., 2009; Tabrizi, Ullmann, Vons, Lafont, & Schmidt-Ott, 2009). For the HT system the carrier gas flow was held constant (at 1.7 l/min) while the generation temperature was either 1625 or 1575 °C. With an increase in generation temperature, the CMD of the aggregate distribution increased, while the width of the distribution remained similar, Table 1. The increase in CMD is explained by an increased evaporation of particle material with temperature, material then available for forming the particles. Accordingly, the output with respect to mass strongly increases with increasing temperature. The mass output here being calculated using DMA–APM data in combination with DMPS. The total aggregate number did not increase as the generation temperature was increased. The HT had a higher output than the SDG$_P$ with regards to both number and mass concentration. The SDG$_C$ system had a similar output as the HT with respect to particle number concentration, while a
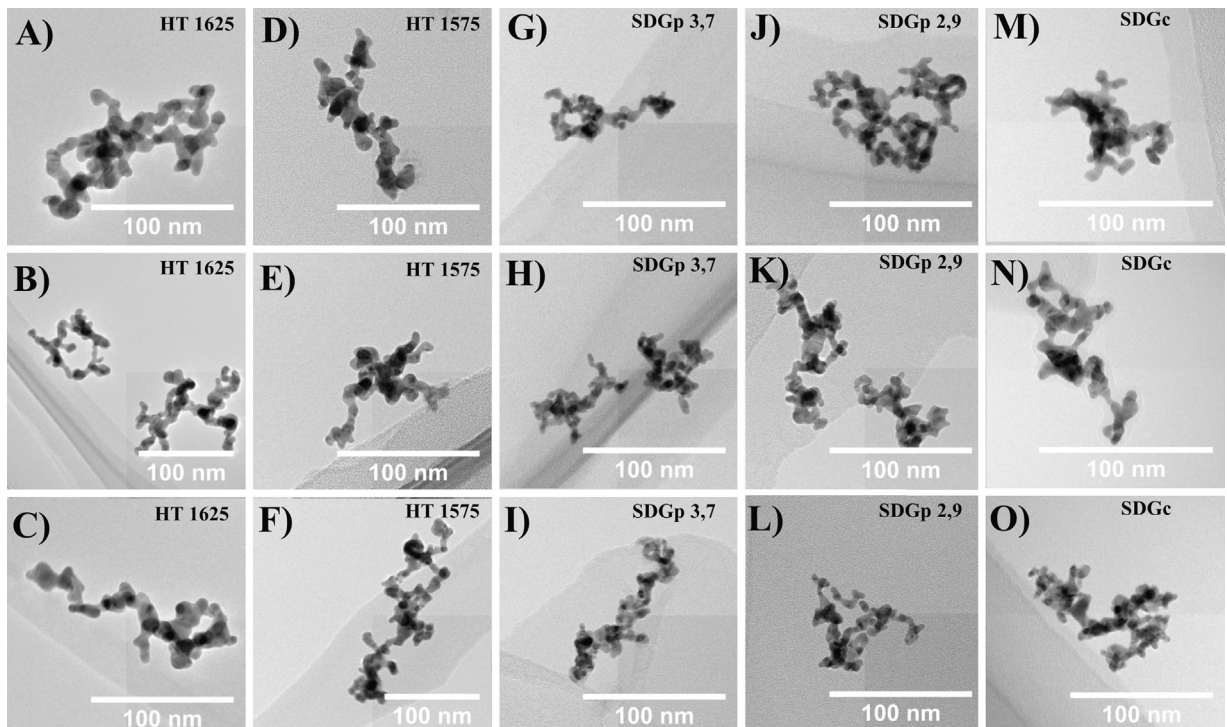
Fig. 4. TEM images of the generated aggregates: (A–C) HT 1625 aggregates, (D–F) HT 1575 aggregates, (G–I) SDG$_P$ 3,7 aggregates, (J–L) SDG$_P$ 2,9 aggregates, and (M–O) SDG$_C$ aggregates.

Table 1

Statistics of the aerosols based on DMPS and DMA–APM measurements. CMD is the count median diameter of the aggregate number size distribution, GSTD the geometric standard deviation and D_{mm} and k fitted parameters to the DMA–APM data (defined in Eq. (5)). The units for mobility diameter and mass used when fitting the parameters in the power law function are [m] and [kg] (SI units). The mass concentration is calculated from the measured number size distribution and mass–mobility relation.

	CMD (nm)	GSTD	Number conc. (#/cm^3)	Mass conc. (mg/m^3)	D_{mm} (95% CI)	k
HT 1625	74.8	1.80	9.28×10^7	48.1	2.35 (95% CI, 2.17–2.54)	54.7×10^{-3}
HT 1575	53.9	1.79	1.19×10^8	34.3	2.23 (95% CI, 1.93–2.52)	6.83×10^{-3}
SDG$_P$ 3.7	28.3	1.65	2.05×10^8	6.08	2.18 (95% CI, 2.11–2.26)	1.39×10^{-3}
SDG$_P$ 2.9	28.1	1.64	1.91×10^8	6.41	2.22 (95% CI, 2.16–2.28)	2.74×10^{-3}
SDG$_C$	78.4	1.92	8.62×10^7	25.0	2.24 (95% CI, 2.13–2.34)	5.23×10^{-3}

slightly lower mass output. The SDG$_C$ had a higher CMD and GSTD compared to both the SDG$_P$ and the HT systems for either setting. Thus, the lower mass output was mainly explained by the lower effective density of the aggregates (discussed later). One of the goals of the SDG$_C$ was to enable the generation of particles with broader size distributions then a commercially available SDG$_P$, and this result confirms that it is possible. The main reason for this is that the SDG$_C$ allows a higher energy input to each spark discharge. It should be mentioned that the out-put of the SDG$_C$ can be increased further by changing settings of the spark discharge.

The mass–mobility relationships (i.e. aggregate mass as a function of mobility diameter) were obtained for each of the systems and settings tested using the DMA–APM technique, Fig. 5. From the mass–mobility relationship, the effective density and dynamic shape factor was determined, defined in Eqs. (6) and (7), and also presented in Fig. 5.

The mass–mobility relationship of the aggregates could in all cases be described by a power law function, Eq. (5). The D_{mm} exponents ranged between 2.18 and 2.35 and are presented in Table 1. Most exponents found were very similar to that suggested in Sorensen (2011) of ∼2.2. One exception was the exponent of particles generated for HT 1625 with a slightly higher of 2.35. This could possibly be explained by the higher temperature during of the aerosol flow resulting in sintering and restructuration. The exponents did however not show any significant differences (CI 95%) between the methods and settings. The data suggest that in order to narrow the confidence interval of D_{mm}, as determined by DMA–APM, more considerations than simply extending the characterization interval should be taken. This is evident when examining the SDG$_C$, SDG$_P$ and HT D_{mm}, the characterization interval for the SDG$_P$ and HT was from 15 to 80 nm and SDGC from 40 to 300 nm. The characterization interval of the SDC$_C$ is in the order 2–3 times wider than SDG$_P$ and HT, while the width of the confidence intervals remain in the same size range.
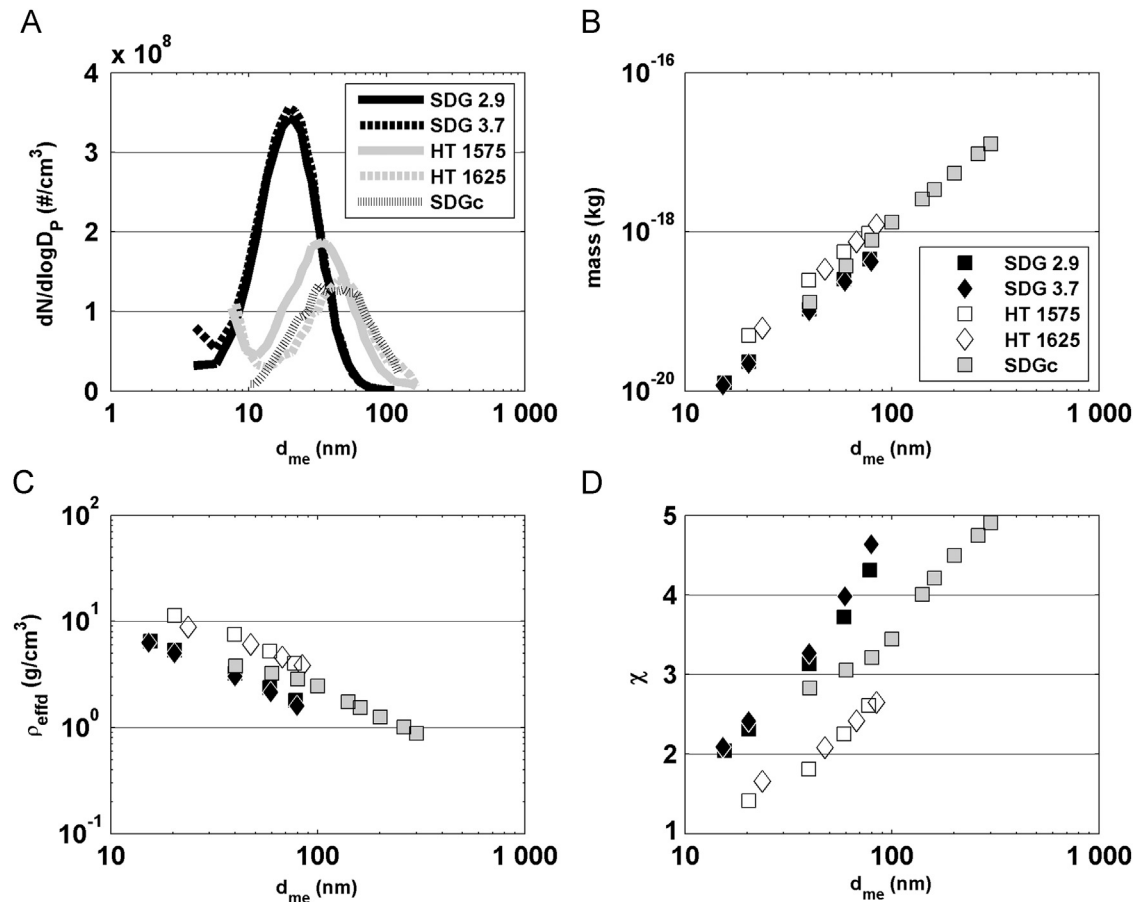
Fig. 5. (A) Aggregate mobility number size distributions for the generated aerosols, (B) mass–mobility relationships for SDGp, HT method and SDGc, (C) effective density, and (D) dynamic shape factor, χ, plotted versus mobility size.

The particle effective density ranged from 15.6 g/cm^3 for the smallest (15 nm) measured aggregates (measured only for the SDG$_P$ system), down to 0.8 g/cm^3 for the 400 nm particles, shown in Fig. 5C. The decrease in effective density over mobility sizes is expected if aggregated particles formed in a diffusion-limited process. Overall, the HT furnace generated more compact aggregates with the highest effective densities. In the size range where HT and SDG$_P$ overlap with SDG$_C$, the SDG$_C$ particle effective densities lay in-between the HT and SDG$_P$ settings (Fig. 5C). The same trends as for effective density is evident in the calculated shape factor (Fig. 5D), defined in Eq. (7).

The total mass of the aggregate distributions were in addition to that previously discussed, DMA–APM in combination with DMPS, calculated by two models based on aggregation theory, as well as when assuming spherical particles of density 19.3 g/cm^3 (gold). The number of primary particles per aggregate was calculated using the theory as described in Sorensen (2011) and that suggested in Lall et al. (2008), as described in Sections 3.2.3 and 3.2.5, and the aggregate mass was calculated as the sum mass of all primary particles in the aggregate. The total aerosol distribution was estimated combining the modeled aggregate mass with the aggregate number size distribution according to the DMPS. In this comparison we expect the DMA–APM derived aerosol mass to be close to the true mass, since based on the measurements only, with no assumptions regarding the aggregate type.

For SDG$_P$ the DMA–APM derived aerosol mass was comparable to that calculated using Sorensen (2011) theory, while the aerosol mass calculated using theory from Lall et al. (2008) was significantly lower for the SDG$_P$. For the HT settings the same trend is evident, DMA-based aerosol mass is the highest followed by that based on Lall et al. (2008) and Sorensen (2011) in declining order. As expected the aerosol mass based on the assumption of spherical particles resulted in the highest mass. This is due to the porous structure of the particles, reflected also in the shape factor and effective density, Fig. 5C and D.

The difference in aerosol mass modeled based on Lall et al. (2008) or on Sorensen (2011) has been observed earlier, and as pointed out in Eggersdorfer, Groehn, Sorensen, McMurry, and Pratsinis (2012) the model suggested in Lall et al. (2008) has several issues. For example, only part of the generated aerosols can be argued to be in the *Kn* regime as required by the Lall and Friedlander theory, that is the free molecular regime.

The differences in modeled aggregate mass based on Sorensen (2011) and the mass estimated based on DMA–APM measurements cannot be fully explained by the occurrence of bridging, explored in Section 5.1.2. Nor can it be explained by

measurement uncertainties of the DMA–APM. One possible explanation for the discrepancy between the DMA–APM based aerosol mass and that of Lall et al. (2008) and Sorensen (2011) could be that the aggregates selected for primary particle image analysis was not representative of the entire aggregate size distribution. Then, since the aggregate number size distributions were different for the different generators, the aggregates analyzed would represent a different fraction of the distributions with regards to primary particle size. This would affect both the Lall et al. (2008) and Sorensen (2011) based aerosol mass since the aggregate mass is the number of primary particles per aggregate, as calculated from the theory, multiplied with the mass of each primary particle (proportional to d_{pp}^3). In this study the TEM images was performed on aggregates of 60 nm mobility size for all methods and settings.

In short, the aggregate surface area was calculated by multiplying the size dependent aggregate mass with the specific surface area, Eqs. (11), (15), (18) and (21). The surface area of the individual aggregates is in turn multiplied with the number of aggregates in the size bin of the number size distribution Eq. (8). Finally, the sum of all bins is the total aerosol surface area of the aerosol, Eq. (9). The surface area of the aerosols were also calculated by assuming the mobility diameter was the true geometrical diameter, as described earlier.

For the SDG$_P$ settings the calculated surface area are similar for Approaches I–III and the approach based on the assumption of spherical particles, while Approach IV predict lower surface areas. For the HT settings and the SDG$_C$ the calculated surface area concentration are more divergent, illustrated in Fig. 6B. Still Approach IV predicts significantly lower values. Approach I predict the highest surface area concentration, followed by Approaches III and II, respectively. The larger differences in predicted surface area is partly explained by the larger size of the aggregates, for which the models differs more than for smaller aggregates.

The difference between Approaches I and III, with regards to total predicted surface area, is explained by the difference in SSA_{TEM} and SSA_{APM}. This is because both approaches use the same size dependent aggregate mass, as determined by DMA–APM. The difference in SSA between Approaches I and III can in turn be traced to the difference in the Sauter primary particle diameter based on TEM and theory (Eggersdorfer, Groehn, Sorensen, McMurry, & Pratsinis, 2012; Eggersdorfer, Kadau, Herrmann, & Pratsinis, 2012), Table 2. When comparing results from Approaches I and III it is clear that even small differences in the Sauter diameter result in substantial differences in total calculated surface area.

In contrast to that described in the previous paragraph, where differences in aerosol surface area could be explained by the used SSA, observed differences between Approaches I, II and IV is explained by the size dependent aggregate mass (as shown in Fig. 6A). Thus, the discussion between the mass predicted by DMA–APM, Lall et al. (2008), and Sorensen (2011) theory is relevant also for the total calculated surface area.

When here applying the surface area Approaches I, II and IV, the same definition of primary particle size is used with regards to SSA. However, it is important to note that depending on how primary particle size is defined, the resulting specific surface area will vary. For primaries of a narrow size distribution this is not an issue. However, most often the primary particles consist of a distribution with some broadening. Thus, how the d_{pp} achieved from the size distribution of primaries (i.e. weighted by nr, area or volume) is critical for the resulting estimate of total surface area. The same holds for estimating the mass of the primaries.

There is no praxis to date as to what weight or derivative from the primary particle distribution that consecutively should be used for surface area calculations, such as Sauter primary particle diameter and SSA.

5.1.2. Primary particle analysis and bridging

The primary particle size and the bridging between the primaries was determined for all generation methods and settings by TEM imagery and subsequent image analysis. Also the Sauter primary particle diameter was calculated from TEM measurements (d_{va-TEM}), Eq. (3). The Sauter diameter was then in its turn used to determine the specific surface area of aggregates (SSA_{TEM}), as presented in previous sections. Results from the primary particle analysis are summarized in Table 2. In addition, a method suggested by Charvet et al. (2014) was tested to predict the d_{pp} from the DMA–APM data as described in Section 2.5.2, here referred to as d_{APM}. Similarly, Eggersdorfer, Groehn, Sorensen, McMurry, and Pratsinis (2012) suggest a method to predict the Sauter primary particle diameter from the DMA–APM data, d_{va-APM}.

There is a clear difference in the diameter of the primaries with regards to the different generation methods, whereas the degree of bridging is similar.

Analysis of the primary particles, based on TEM, shows that the HT method results in the largest primary particles for all types of d_{pp} (nr, area and volume). The temperature of the furnace did not seem to affect the primary particle size to any great extent. The SDG$_P$ generator produced aggregates with a lower primary particle size than the HT method with regards to all approaches determining the primary particle size, and did not change considerably with the carrier gas flow rate in the flow range measured. The primary particle size of the SDG$_C$ by TEM was similar to that of the SDG$_P$ generator.

The primary particle size predicted from DMA–APM data (d_{APM}, d_{va-APM}) in general predict larger differences of the primary particles than what can be observed from the TEM image analysis. It is apparent that the similarity in primary particle size, as determined from TEM, for SDG$_P$ and SDG$_C$ aggregates is not present for d_{APM} and d_{va-APM}. This most likely reflect the effective densities (Fig. 5), where the effective density of the SDG$_C$ lies between that of SDG$_C$ and HT. The Sauter primary particle sizes calculated from DMA–APM, d_{va-APM}, are in general larger than those based on TEM, d_{va-TEM}, for HT and SDG$_C$. A possible explanation could be that the aggregates formed by the HT and SDG$_C$ are of a more compact structure than those formed by SDG$_P$, erroneously interpreted as larger primary particles.
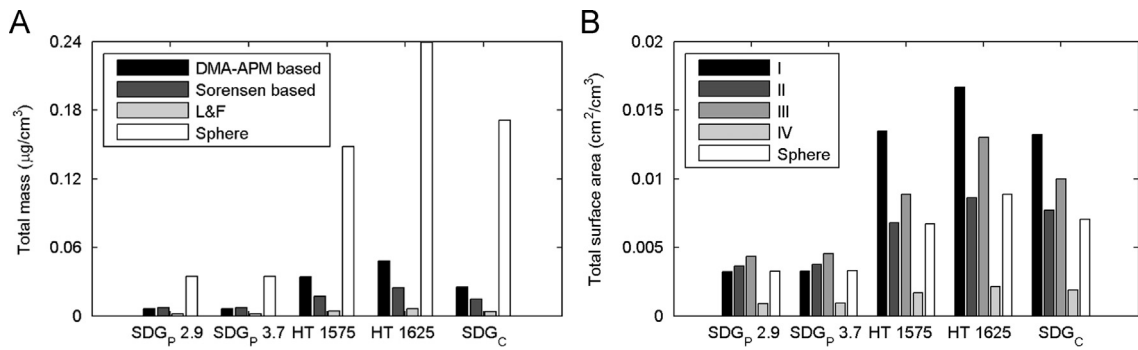
Fig. 6. (A) Comparison of calculated total mass of the characterized aerosols based on DMA–APM measurements to that of modeled using DCLA-theory of Sorensen (2011), Lall et al. (2008) and assuming that the particles are spherical with density 19.3 g/cm³. (B) The total surface area for each method and setting was calculated using each of the Approaches I–IV respectively, the approaches defined in Sections 3.2.2–3.2.5, including a calculation based on the assumption that the mobility diameter is the true physical diameter.

Table 2
Primary particle analysis and specific surface area based on TEM image analysis (i.e. on $d_{va\text{-}TEM}$) and DMA–APM data, as described in material and methods. N_{pp} refer to the number of measured primary particles for each generation method and settings. The average diameter (μ) is estimated both from number, surface area and mass weighted distributions.

Primary particle size, bridging analysis and *SSA* based on TEM

	N_{PP}	μ (nm $\pm$ std)			$d_{va\text{-}TEM}$	SSA_{TEM} (m²/g)	b_r (std)
		Nr	Area	Vol			
HT 1625	482	8.26 $\pm$ 2.07	8.68 $\pm$ 2.29	9.36 $\pm$ 2.26	8.98	34.63	0.70 $\pm$ 0.08
HT 1575	604	7.31 $\pm$ 1.69	7.71 $\pm$ 1.76	8.29 $\pm$ 1.78	7.92	39.24	0.64 $\pm$ 0.09
SDG$_p$ 3.7	373	5.41 $\pm$ 1.34	5.74 $\pm$ 1.41	6.11 $\pm$ 1.41	5.82	53.46	0.64 $\pm$ 0.11
SDG$_p$ 2.9	486	5.79 $\pm$ 1.32	6.11 $\pm$ 1.27	6.36 $\pm$ 1.35	6.20	50.18	0.62 $\pm$ 0.11
SDG$_c$	310	5.55 $\pm$ 1.35	5.83 $\pm$ 1.37	6.17 $\pm$ 1.32	5.89	52.74	0.66 $\pm$ 0.09

Primary particle size derived from DMA–APM data

	d_{APM}[a]		$d_{va\text{-}APM}$[b]	SSA_{APM} (m²/g)[c]
	(nm)	(nm $\pm$ SE)	(nm)	(m²/g)
HT 1625	7.34	$e^{(1.99 \pm 0.13)}$	11.49	27.06
HT 1575	10.74	$e^{(2.37 \pm 0.13)}$	12.01	25.89
SDG$_p$ 3.7	3.92	$e^{(1.37 \pm 0.07)}$	4.18	74.37
SDG$_p$ 2.9	3.92	$e^{(1.37 \pm 0.06)}$	4.58	67.88
SDGc	5.76	$e^{(1.75 \pm 0.17)}$	7.80	39.86

[a] From measured effective density analysis and density of the pure compound according to the method suggested in Charvet et al. (2014).
[b] Method suggested in Eggersdorfer, Groehn, Sorensen, McMurry, and Pratsinis (2012).
[c] Based on $d_{va\text{-}APM}$.

In the model suggested in Charvet et al. (2014) to determine the primary particle size (d_{APM}), the power-law function fitted to the effective density over mobility diameter is extrapolated down to the size of the primary particles (i.e. when the effective density reaches the material crystal density). To our understanding, this assumption is acceptable for aggregates formed by DLCA, but only for $N > 100$ (Sorensen, 2011). Nevertheless, comparing the results of the d_{pp} predicted from DMA–APM they correlate relatively well, with the exception of the HT 1625.

5.1.3. Model sensitivity of bridging

The TEM image analysis shows that the ratio between the diameter of the bridge and adjacent primary particles was similar for all methods and settings tested, around 60–70% (b_r 0.6–0.7). Using this as input in a sensitivity study of bridging on estimated specific surface area, the assumption of point contact lead to an overestimation of specific surface area by ~20% (20% using method A and 22% for B). The effect of the bridging is calculated assuming the two geometries (A and B) resulting from the two assumptions of how the bridging is formed, described in Section 2.5.3. As can be seen the two assumptions resulted in similar values. Assuming the extreme – that the diameter ratio of the bridge and primary particles are unity – will result in an overestimation of the specific surface area by 50%.

Bau et al. (2010) also suggest a method to compensate for bridging in the determination of specific surface area from TEM image analysis by introducing an overlap coefficient. Estimating the corresponding overlap coefficient corresponding to a b_r of 0.6 and 0.7, respectively, assuming that the primary particles fuse together (method B), result in coefficients of 0.096 and

Table 3
Overview of the input needed (empirical or theoretical) for surface area estimations using the four different approaches.

Approach	I	II	III	IV
DMA–APM	X		X	
TEM	X	X		X
DLCA		X	X	X

0.134, respectively. Neglecting this overlap coefficient, results in overestimating the specific surface area by ~14–21% (from the equations given by Bau et al. (2010), which is similar to the 20% achieved from the above approach.

When estimating the aggregate surface area based on aggregation theory using Approach II, the effect on surface area is more complex. The specific surface area will be affected in the same way as described above. However, also when predicting the aggregate mass–mobility relationship from aggregation theory, the bridging will come into account and shift d_{me} compared to that of pure aggregates. If the bridging is formed according to method A, the volume/mass of the aggregates will be underestimated using the assumption of point contact. This is because material condenses onto the aggregates after they have formed according to DLCA. On the other hand, d_{me} will be shifted towards larger sizes during the condensation process, and will counteract the total effect on the mass–mobility relationship. If instead the formation of the bridge is described by method B, the mass of a specific aggregate will be the same as that predicted by the theory; however d_{me} will in this case be shifted towards smaller mobility diameters during the fusing of the primary particles.

5.2. Discussion of surface area approaches

The surface area of individual aggregates as a function of d_{me} are calculated using the four approaches described in Section 2, as well as assuming spherical particles. An overview of the approaches and what they are based on is provided in Table 3.

When choosing an approach to estimate the surface area of an aerosol it is important to consider limitations, pros and cons, and of course the instruments that are available. Regarding Approaches II and IV an advantage is that a DMA–APM measurement is not needed. It does however require a primary particle image analysis, for example by TEM. In contrast, Approach III does not require a primary particle analysis, while it does require DMA–APM measurements of the aerosol.

Approach II is strictly limited to aggregates formed by DLCA with no following restructuring occurring. Approach III is limited to aggregates formed by DLCA and sintered by viscous flow, grain boundary or lattice diffusion. Many aerosol aggregate distributions have large portions that are not in the free molecular regime, for example combustion soot or welding fume, making Approach IV unsuitable. It is unlikely that these approaches (II, III and IV) describe the properties of aggregates formed from abrasion or dustiness, or aggregates that restructure upon, for example, humidification. Approach I requires both DMA–APM and primary particle image analysis. However, it is not limited to the shape of the aggregates and thus applies to aggregates of all forms and not only to aggregates formed by DLCA. Thus, the method can be used for all types of aggregates. In all approaches bridging needs to be considered, as discussed in Section 5.1.3.

6. Conclusions

The characteristics and output of gold aggregates generated by three methods at different settings were tested. The aggregates were investigated using both online techniques (DMPS, DMA–APM) as well as off-line (TEM). The generators used were a new custom-built spark discharge generator (SDG$_C$), a commercially available spark discharge system (SDG$_P$), and a high temperature evaporation furnace (HT). The output of the SDG$_C$, with respect to both mass and surface area was higher than for the SDG$_P$. Furthermore, the distributions were broader than for both the SDG$_P$ and HT. This, together with a compact system design, makes the new system preferable in a number of applications ranging from in vivo and in-vitro tests of toxicity to calibration of in-situ techniques – where it often is required to move the system between sites and in which a high output over a broad size range is preferable to allow tuning.

The mass–mobility relationship indicates that all characterized aerosols are highly aggregated. This is confirmed by TEM image analysis showing a typical diameter of the primary particles of 6–9 nm. The aggregates had clear bridges between the primaries (60–70% of the diameter of the primary particles), similar for all methods and settings tested. Analysis of the mass–mobility relation for the Gold aerosols showed that it can be well described by a power law with mass–mobility exponents in the range of 2.18–2.34. Interestingly the confidence interval (95%) show that they are not significantly distinguished between the methods i.e. no significant difference in D_{mm} can be asserted. With regards to reducing the uncertainty in D_{mm} it is clear that a wider span of DMA–APM characteristics does not on its own narrow the confidence interval.

The HT methods for both settings produce aggregates of a higher mass as compared to the other methods at a given mobility size. This property is also reflected in the effective density and the calculated shape factor. The higher effective densities can partly be explained by larger primary particle sizes. However, when comparing the measured effective densities with that estimated from aggregation theory (DCLA; Sorensen, 2011), it seems that the primary particle size does

not fully explain the observed difference. That the difference is due to difference in bridging can be ruled out and the deviation is larger than the uncertainty in the measured effective density. One hypothesis could be that the aggregates selected for primary particle image analysis is not representing the entire aggregate size distribution and that the primary particle size is not the same over the aggregate size distribution. One could also speculate that the properties of the aggregates formed in the different generator really have a difference in structure.

With regards to the predicted surface area of the characterized aerosols, the difference varied with at most a factor of 2 between the approaches, excluding Approach IV, for one and same generation method and setting. Including Approach IV there was as most a factor of 8 in difference for HT 1625, approach I highest with Approach IV predicting the lowest surface area.

For the SDG_P settings the difference is surprisingly small for the calculated surface areas, excluding Approach IV, and is partly explained by the low CMD of the distributions. For distributions containing larger aggregates the differences is expected to be larger. Approach I predict a slightly lower total surface area for the SDG_P aerosols as compared to Approaches II and III. However, for the HT and SDG_C aerosols Approach I instead predict a considerably higher total surface area. The difference in predicted surface area between Approaches I, II and IV reflects the difference in aggregate mass, since the approaches use the same specific surface area SSA_{TEM} in their method. The difference between Approaches I and III is instead explained by the difference in specific surface, while they both use the same aggregate mass in the calculations.

As expected, since the generated aerosol was shown to be aggregated, the aerosol mass based on the assumption of sphericity was significantly higher as compared to that based on DMA–APM, Lall et al. (2008) and Sorensen (2011). The aerosol surface area based on the same assumption was comparable to the other approaches, especially Approach II.

In order to fully understand and describe the observations a more advanced image analysis technique could be very useful. This is because a large part of the investigated aggregates, as apparent from Fig. 4, cannot be described by primary particles. Furthermore, more TEM-samples would be needed, collected for aggregates of more than one mobility size. A more representative selection could be aggregates of the mobility diameter where each distribution peaks.

7. Data sharing

The data that this study is based upon is publicly available through Swedish National Data Service (www.SND.gu.se/en) by doi:10.5878/002624. Data available are those related to Fig. 5 i.e. mobility to mass/effective density/shape factor. Also data from the primary particle analysis using imageJ is appended for each of the methods.

It is the hope of the authors that the data will be a valuable asset and live on in research to come.

Acknowledgments

References

Aitken, R., Chaudhry, M., Boxall, A., & Hull, M. (2006). Manufacture and use of nanomaterials: current status in the UK and global trends. *Occupational Medicine*, 56(5), 300–306.

Asbach, C., Fissan, H., Stahlmecke, B., Kuhlbusch, T., & Pui, D. (2009). Conceptual limitations and extensions of lung-deposited Nanoparticle Surface Area Monitor (NSAM). *Journal of Nanoparticle Research*, 11(1), 101–109.

Barath, S., Mills, N.L., Lundback, M., Tornqvist, H., Lucking, A.J., & Langrish, J.P., et al. (2010). Impaired vascular function after exposure to diesel exhaust generated at urban transient running conditions. *Particle and Fibre Toxicology*, 7(19), 1–11.

Bau, S., Witschger, O., Gensdarmes, F., Rastoix, O., & Thomas, D. (2010). A TEM-based method as an alternative to the BET method for measuring off-line the specific surface area of nanoaerosols. *Powder Technology*, 200(3), 190–201.

Brunauer, S., Emmett, P.H., & Teller, E. (1938). Adsorption of gases in multimolecular layers. *Journal of the American Chemical Society*, 60(2), 309–319.

Chan, P., & Dahneke, B. (1981). Free-molecule drag on straight chains of uniform spheres. *Journal of Applied Physics*, 52(5), 3106–3110.

Charvet, A., Bau, S., Paez Coy, N., Bémer, D., & Thomas, D. (2014). Characterizing the effective density and primary particle diameter of airborne nanoparticles produced by spark discharge using mobility and mass measurements (tandem DMA/APM). *Journal of Nanoparticle Research*, 16(5), 1–11.

Dahneke, B. (1982). Viscous resistance of straight-chain aggregates of uniform spheres. *Aerosol Science and Technology*, 1(2), 179–185.

Deppert, K., Schmidt, F., Krinke, T., Dixkens, J., & Fissan, H. (1996). Electrostatic precipitator for homogeneous deposition of ultrafine particles to create quantum-dot structures. *Journal of Aerosol Science*, 27(1001), 151–152.

DFG (2013). *Nanomaterials*. Wiley-VCH Verlag GmbH & Co. KGaA: .

Dillon, F., Copley, M., Koos, A.A., Bishop, P., & Grobert, N. (2013). Flame spray pyrolysis generated transition metal oxide nanoparticles as catalysts for the growth of carbon nanotubes. *RSC Advances*, 3(43), 20040–20045.

Dockery, D.W., Pope, C.A., Xu, X.P., Spengler, J.D., Ware, J.H., & Fay, M.E., et al. (1993). An association between air-pollution and mortality in 6 United-States Cities. *New England Journal of Medicine*, 329(24), 1753–1759.

Donaldson, K., Borm, P.J.A., Oberdorster, G., Pinkerton, K.E., Stone, V., & Tran, C.L. (2008). Concordance between in vitro and in vivo dosimetry in the proinflammatory effects of low-toxicity, low-solubility particles: The key role of the proximal alveolar region. *Inhalation Toxicology*, 20(1), 53–62.

Eggersdorfer, M.L., Groehn, A.J., Sorensen, C.M., McMurry, P.H., & Pratsinis, S.E. (2012). Mass-mobility characterization of flame-made ZrO2 aerosols: Primary particle diameter and extent of aggregation. *Journal of Colloid and Interface Science*, 387, 12–23.

Eggersdorfer, M.L., Kadau, D., Herrmann, H.J., & Pratsinis, S.E. (2012). Aggregate morphology evolution by sintering: number and diameter of primary particles. *Journal of Aerosol Science*, 46, 7–19.

Ehara, K., Hagwood, C., & Coakley, K.J. (1996). Novel method to classify aerosol particles according to their mass-to-charge ratio – Aerosol particle mass analyser. *Journal of Aerosol Science*, 27(2), 217–234.

Fierz, M., Houle, C., Steigmeier, P., & Burtscher, H. (2011). Design, calibration, and field performance of a miniature diffusion size classifier. *Aerosol Science and Technology*, 45(1), 1–10.

Gopalakrishnan, R., Thajudeen, T., Ouyang, H., & Hogan, C.J. (2013). The unipolar diffusion charging of arbitrary shaped aerosol particles. *Journal of Aerosol Science*, 64, 60–80.

Heurlin, M., Magnusson, M.H., Lindgren, D., Ek, M., Wallenberg, L.R., & Deppert, K., et al. (2012). Continuous gas-phase synthesis of nanowires with tunable properties. *Nature*, 492(7427), 90–94.

Karlsson, M.N.A., Deppert, K., Karlsson, L.S., Magnusson, M.H., Malm, J.O., & Srinivasan, N.S. (2005). Compaction of agglomerates of aerosol nanoparticles: A compilation of experimental data. *Journal of Nanoparticle Research*, 7(1), 43–49.

Knutson, E.O., & Whitby, K.T. (1975). Aerosol classification by electric mobility: apparatus, theory, and applications. *Journal of Aerosol Science*, 6(6), 443–451.

Ku, B.K., & Kulkarni, P. (2012). Comparison of diffusion charging and mobility-based methods for measurement of aerosol agglomerate surface area. *Journal of Aerosol Science*, 47, 100–110.

Ku, B.K., & Maynard, A.D. (2005). Comparing aerosol surface-area measurements of monodisperse ultrafine silver agglomerates by mobility analysis, transmission electron microscopy and diffusion charging. *Journal of Aerosol Science*, 36(9), 1108–1124.

Lall, A.A., & Friedlander, S.K. (2006). On-line measurement of ultrafine aggregate surface area and volume distributions by electrical mobility analysis: I. Theoretical analysis. *Journal of Aerosol Science*, 37(3), 260–271.

Lall, A.A., Rong, W., Mädler, L., & Friedlander, S.K. (2008). Nanoparticle aggregate volume determination by electrical mobility analysis: Test of idealized aggregate theory using aerosol particle mass analyzer measurements. *Journal of Aerosol Science*, 39(5), 403–417.

LeBouf, R.F., Ku, B.K., Chen, B.T., Frazer, D.G., Cumpston, J.L., & Stefaniak, A.B. (2011). Measuring surface area of airborne titanium dioxide powder agglomerates: Relationships between gas adsorption, diffusion and mobility-based methods. *Journal of Nanoparticle Research*, 13(12), 7029–7039.

Lövestam, G., Rauscher, H., Roebben, G., Klüttgen, B.S., Gibson, N., & Putaud, J.-P., et al. (2010). *Considerations on a definition of nanomaterial for regulatory purposes. Joint Research Centre (JRC) Reference Reports*. IHCP: .

McMurry, P.H., Wang, X., Park, K., & Ehara, K. (2002). The relationship between mass and mobility for atmospheric particles: A new technique for measuring particle density. *Aerosol Science and Technology*, 36(2), 227–238.

Meakin, P., Donn, B., & Mulholland, G.W. (1989). Collisions between point masses and fractal aggregates. *Langmuir*, 5(2), 510–518.

Messing, M., Svensson, C.R., Pagels, J., Meuller, B.O., Deppert, K., & Rissler, J. (2012). Gas-borne particles with tunable and highly controlled characteristics for nanotoxicology studies. *Nanotoxicology*, 7(6), 1052–1063.

Messing, M.E., Dick, K.A., Wallenberg, L.R., & Deppert, K. (2009). Generation of size-selected gold nanoparticles by spark discharge – For growth of epitaxial nanowires. *Gold Bulletin*, 42(1), 20–26.

Meuller, B.O., Messing, M.E., Engberg, D.L., Jansson, A.M., Johansson, L.I., & Norlén, S.M., et al. (2012). Review of spark discharge generators for production of nanoparticle aerosols. *Aerosol Science and Technology*, 46(11), 1256–1270.

Ntziachristos, L., Giechaskiel, B., Ristimäki, J., & Keskinen, J. (2004). Use of a corona charger for the characterisation of automotive exhaust aerosol. *Journal of Aerosol Science*, 35(8), 943–963.

Olfert, J., Symonds, J., & Collings, N. (2007). The effective density and fractal dimension of particles emitted from a light-duty diesel vehicle with a diesel oxidation catalyst. *Journal of Aerosol Science*, 38(1), 69–82.

Park, K., Kittelson, D.B., & McMurry, P.H. (2004). Structural properties of diesel exhaust particles measured by transmission electron microscopy (TEM): Relationships to particle mass and mobility. *Aerosol Science and Technology*, 38(9), 881–889.

Rasband, W. (1997–2012). *WS 1997–2012 ImageJ*. US National Institutes of Health: Bethesda, Maryland, USA.

Rissler, J., Messing, M.E., Malik, A.I., Nilsson, P.T., Nordin, E.Z., & Bohgard, M., et al. (2013). Effective density characterization of soot agglomerates from various sources and comparison to aggregation theory. *Aerosol Science and Technology*, 47(7), 792–805.

Rissler, J., Nordin, E.Z., Eriksson, A.C., Nilsson, P.T., Frosch, M., & Sporre, M.K., et al. (2014). Effective density and mixing state of aerosol particles in a near-traffic urban environment. *Environmental Science & Technology*, 48(11), 6300–6308.

Rissler, J., Swietlicki, E., Bengtsson, A., Boman, C., Pagels, J., & Sandström, T., et al. (2012). Experimental determination of deposition of diesel exhaust particles in the human respiratory tract. *Journal of Aerosol Science*, 48, 18–33.

Scheibel, H.G., & Porstendorfer, J. (1983). Generation of monodisperse Ag-aerosol and NaCl-aerosol with particle diameters between 2-N m and 300-N m. *Journal of Aerosol Science*, 14(2), 113–126.

Schwyn, S., Garwin, E., & Schmidtott, A. (1988). Aerosol generation by spark discharge. *Journal of Aerosol Science*, 19(5), 639–642.

Shin, W.G., Mulholland, G.W., Kim, S.C., Wang, J., Emery, M.S., & Pui, D.Y.H. (2009). Friction coefficient and mass of silver agglomerates in the transition regime. *Journal of Aerosol Science*, 40(7), 573–587.

Sorensen, C.M. (2011). The mobility of fractal aggregates: A review. *Aerosol Science and Technology*, 45(7), 765–779.

Svensson, C.R., Messing, M.E., Lundqvist, M., Schollin, A., Deppert, K., & Pagels, J.H., et al. (2013). Direct Deposition of Gas Phase Generated Aerosol Gold Nanoparticles into Biological Fluids-Corona Formation and Particle Size Shifts. *PloS one*, 8(9).

Tabrizi, N., Xu, Q., van der Pers, N., Lafont, U., & Schmidt-Ott, A. (2009). Synthesis of mixed metallic nanoparticles by spark discharge. *Journal of Nanoparticle Research*, 11(5), 1209–1218.

Tabrizi, N., Xu, Q., van der Pers, N., & Schmidt-Ott, A. (2010). Generation of mixed metallic nanoparticles from immiscible metals by spark discharge. *Journal of Nanoparticle Research*, 12(1), 247–259.

Tabrizi, N.S., Ullmann, M., Vons, V., Lafont, U., & Schmidt-Ott, A. (2009). Generation of nanoparticles by spark discharge. *Journal of Nanoparticle Research*, 11(2), 315–332.

Thajudeen, T., Jeon, S., & Hogan, C.J. (2015). The mobilities of flame synthesized aggregates/agglomerates in the transition regime. *Journal of Aerosol Science*, 80, 45–57.

Wang, J., Shin, W., Mertler, M., Sachweh, B., Fissan, H., & Pui, D. (2010). Measurement of nanoparticle agglomerates by combined measurement of electrical mobility and unipolar charging properties. *Aerosol Science and Technology*, 44(2), 97–108.

Waters, K.M., Masiello, L.M., Zangar, R.C., Zangar, R.C., Karin, N.J., & Quesenberry, R.D., et al. (2009). Macrophage responses to silica nanoparticles are highly conserved across particle sizes. *Toxicological Sciences*, 107(2), 553–569.

Wiedensohler, A. (1988). An approximation of the bipolar charge-distribution for particles in the sub-micron size range. *Journal of Aerosol Science*, 19(3), 387–389.